# Parametric Analysis on the Static and Modal Response of Folded Metamaterials

IOP Conf. Series: Materials Science and Engineering 1306 (2024) 012037 doi:10.1088/1757-899X/1306/1/012037

# Parametric Analysis on the Static and Modal Response of Folded Metamaterials

**P.M. Santucci and A. Baldi**

University of Cagliari, Department of Mechanical, Chemical and Materials Engineering, Via Marengo 2, 09123 Cagliari, Italy

E-mail: pietrom.santucci@unica.it

**Abstract.** Metamaterials have been studied and analyzed in the past three decades because of their outstanding properties. Generally speaking, a metamaterial is a material that exhibits a mechanical behavior that does not depend only on the bulk material but also on the geometrical configuration in which it lies. This aspect leads to the possibility of tuning and engineering the structural response. One of the most interesting properties is the auxetic behavior of metamaterial. An auxetic material shows a global negative Poisson's ratio. Shock absorption, acoustic dissipation, and shape morphing are some of the most popular employment for auxetic materials. In this article, we focus on the response of folded material under static and dynamic load conditions. Folded materials consist of folding a sheet under specific geometrical constraints. One of the most famous is the Miura-ori pattern, which comes from the origami-folding technique. The geometrical parameters, such as folding angles and edge lengths, play a fundamental role in achieving the desired auxetic behavior. These geometrical parameters define a unit cell that can be stacked into a periodic structure. This article proposes an experimental parametric study of the thickness impact on the auxetic behavior while edge dimensions and folding angles are fixed. The geometrical complexity of the pattern forced us to use additive manufacturing for the specimen fabrication. In particular, we choose Fused Filament Fabrication (FFF) using polymers like ABS and PLA. Digital Image Correlation (DIC) is used for monitoring the displacement and strain fields onto the Miura-ori surface under tensile load. Finally, Time Averaged Speckle Interferometry is employed for evaluating the modal response by using a quasi-full out-of-plane sensitivity setup.

## 1. Introduction

Metamaterials have been the main focus of a solid mechanics branch for several decades. Their name suggests the potential for engineering application: the challenge is the mechanical response control by working on the geometrical configuration rather than the bulk material. In this landscape, the auxetic behavior is still one of the most searched and studied [1–4]. Examples of "naturally" auxetic materials are biological tissues [5–7], cubic metals [8] and several crystals [9, 10]. The auxetic response can be achieved using several strategies, such as two or three-dimensional lattices [11, 12], reentrant structures [13–16], structures with cut slots [17–20], or custom-shape inclusions [21, 22], instability [23–25] and many others [26–28].

Within the family of auxetic materials, the folded ones have been regarded as groundbreaking since their possible applications in several engineering fields [29]. These materials come along with the Japanese origami folding paper technique. The first reference of such a structure is due to Koryo Miura[30], who developed the Miura-ori folding (Figure 1a): it is obtained by

surface tessellation using parallelograms to form the faces. The light weight of these structures and the capacity to deploy made them quite interesting in the aerospace[31] and automotive [32] fields. The energy absorption properties [33, 34] and the possibility of stacking Miura-ori layers in sandwich core composites [35, 36] are other remarkable applications for this geometry.

Thus, the Miura-ori structural response, focusing on the auxetic behavior, has been studied from a kinematic perspective [37, 38]. The kinematical model considers the face skeleton as a rigid articulate parallelogram, concentrating the elastic behavior on the creases [39]. Therefore, the faces rotate relatively around creases. This article proposes an experimental evaluation of thickness influence regarding the auxetic response of a Miura-ori sample under static tensile load. In addition, the modal response of a thick Miura-ori specimen is evaluated by employing interferometric experimental analysis. The article is organized as follows. Section 2 introduces the Miura-ori unit cell, with its geometrical parameters and manufacturing techniques. Section 3 presents the experimental techniques used in the investigation process. Section 3.1 reports more details about the Digital Image Correlation, while section 3.2 focuses on the Time-Averaged Speckle Interferometry. Finally, section 4 presents the experimental results of the parametric analysis on thickness impact and the modal response.

## 2. Model and Methods

The Miura-ori is a folded metamaterial that exhibits an auxetic behavior under specific geometrical prescriptions.

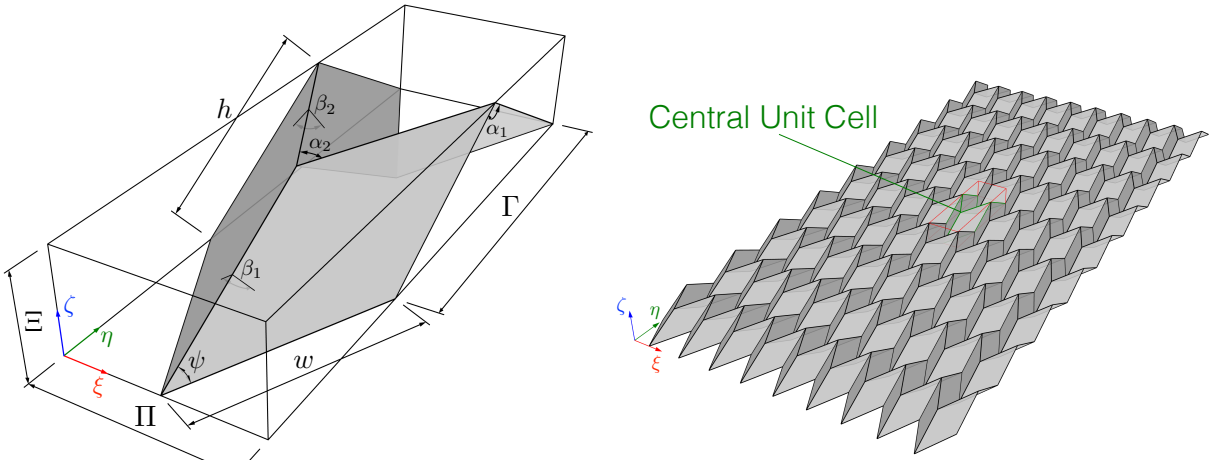


**(a)** *Miura-ori unit cell.* **(b)** *Miura-ori periodic pattern.*

**Figure 1:** *Miura-ori geometry. a) Fundamental parameters of a Miura-ori unit cell. b) Periodic disposition of* $9 \times 9$ *Miura-ori unit cell.*

Figure 1a shows the fundamental geometrical parameters that describe the Miura-ori unit cell: it can be defined using the length of the edges $w$ and $h$, and the folding angles $\alpha_1$ and $\alpha_2$. However, angles $\beta_1$, $\beta_2$, and $\psi$ represent another parameter set, expressed by the following relationships [39]:

$$\cos(\psi) = \sin\left(\frac{\alpha_1}{2}\right)\cos\left(\frac{\alpha_2}{2}\right) \tag{1}$$

$$\cos(\beta_1) = \frac{\cos(\alpha_1) + \cos(\alpha_2)\left[\cos(\alpha_1) + 3\right] - 1}{\cos(\alpha_1) + \cos(\alpha_2)\left[\cos(\alpha_1) - 1\right] + 3} \tag{2}$$

$$\cos(\beta_2) = \frac{\cos(\alpha_2) - \cos(\alpha_1)\left[\cos(\alpha_2) - 3\right] + 1}{\cos(\alpha_1) + \cos(\alpha_2)\left[\cos(\alpha_1) - 1\right] + 3} \tag{3}$$

The unit cell outer dimensions $\Gamma$, $\Pi$ and $\Xi$ are defined as:

$$\Gamma = (2w)\sin\left(\frac{\alpha_1}{2}\right) \tag{4}$$

$$\Pi = (2h)\sin\left(\frac{\alpha_2}{2}\right) \tag{5}$$

$$\Xi = (w)\cos\left(\frac{\alpha_1}{2}\right) \tag{6}$$

The replication of the unit cell along the $\xi$ and $\eta$ axis leads to a periodic pattern of $9 \times 9$ cells, as reported in Figure 1b.

The article of Schenk et al. [37] shows a strong relation, limited to the in-plane analysis, between the Poisson's ratios $\nu_{\eta\xi}$ ($\nu_{\xi\eta}$) and the angle $\alpha_2$, which holds for a kinematical analysis of the deformation mode (eqs. (7) and (8)).

$$\nu_{\eta\xi} = -\frac{1}{\tan^2\left(\frac{\alpha_2}{2}\right)} \tag{7}$$

$$\nu_{\xi\eta} = -\tan^2\left(\frac{\alpha_2}{2}\right) \tag{8}$$

The aforementioned kinematical approach is based on modeling the edges as discontinuity between adjacent faces (Figure 2a), which can relatively rotate around them [37, 39].

In this article, we investigate, from the experimental side, the mechanical response of a Miura-ori structure whose thickness is not negligible (Figure 2b).

A first experimental campaign is oriented to study the influence of thickness on the in-plane auxetic response of Miura-ori periodic structure.

Figure 3a shows a specimen designed for tensile test. The main periodic pattern is composed by $9 \times 9$ thick unit cell, with additional two rows at the top and bottom of the structure: those are used as a connection to the gripping ends. The manufacturing process of these patterns is remarkably challenging because of the sharp elements that discourage conventional manufacturing techniques. Additive manufacturing proved to be a good solution for Miura-ori manufacturing. In particular, Fused Filament Fabrication (FFF) has been employed: the specimens have been printed along $\xi$ axis to avoid any material deposition at cell vertices (Figure 3b). The printer used for manufacturing the samples is a Prusa i3 MK2. The materials employed in the experimental campaign are Polylactic Acid (PLA) and Acrylonitrile Butadiene Styrene (ABS), commonly used polymers in 3D printing. The gripping ends must be stiffer than the rest of the pattern because of the polymeric material: this requirement avoids deformation localization on the ends. Thus, a prismatic slot with reference surfaces guarantees an easier alignment in the tensile test machine (Figure 3a and 5a). In addition, M6 nuts are inserted in the specimen heads,

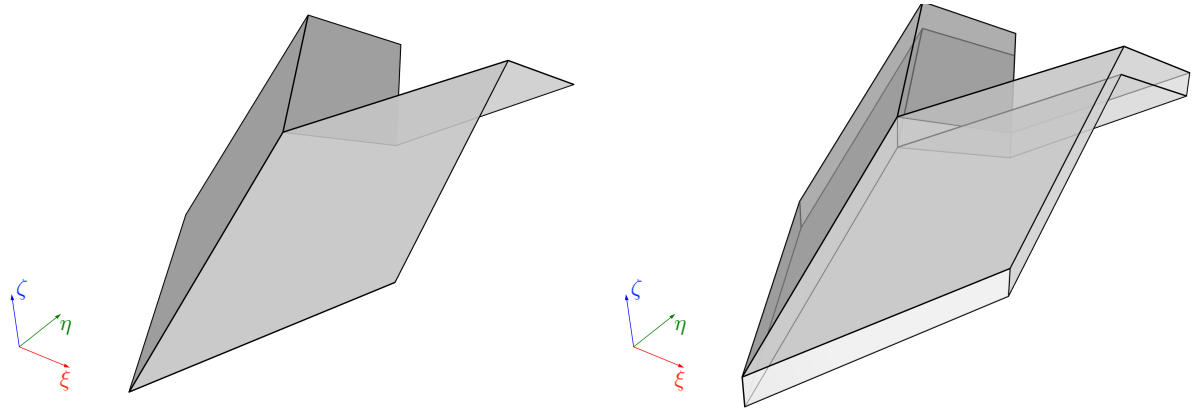


**(a)** *Kinematical model.* **(b)** *Continuum model.*

**Figure 2:** *Comparison between the two unit cell in terms of facets thickness. a) Miura-ori unit cell with negligible facets thickness: the in-plane response is only kinematics related. b) Miura-ori unit cell with a not negligible facets thickness: the in-plane mechanical response is modeled using the continuum mechanics theory.*

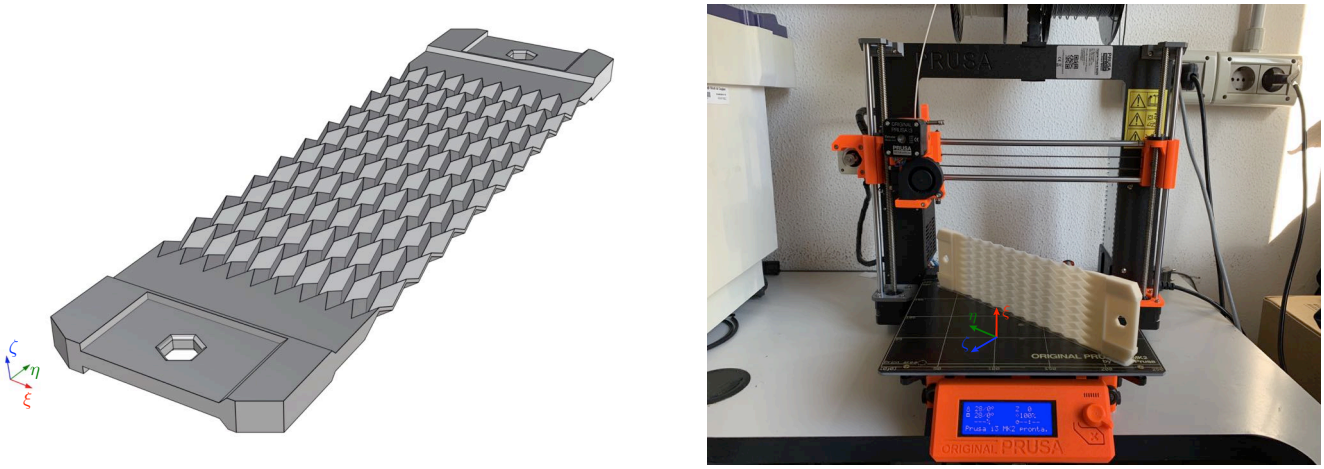


**(a)** *Specimen geometry.* **(b)** *3D printing process.*

**Figure 3:** *Specimen design and fabrication. a) Characteristics of a custom Miura-ori specimen made of* $9 \times 9$ *active cells. b) Manufacturing of a specimen using a Prusa i3 MK2 3D printer.*

where the grips exert their pressure: the nuts act as stroke-end for the grips, avoiding dangerous stress concentration, and preventing the loss of structural integrity due to material failure.

Then, a second campaign focuses on the modal response of such structures. The specimen has the same geometrical characteristics as the one used for the tensile test. It only differs from the previous by the number of cells, which is reduced, for room reasons, to 7 cells along $\eta$ axis and 9 cells along $\xi$ axis.

## 3. Experimental Techniques and Setup

Two different experimental techniques have been used for investigating the mechanical response under tensile tests and the modal response. Digital Image Correlation (DIC) has been employed

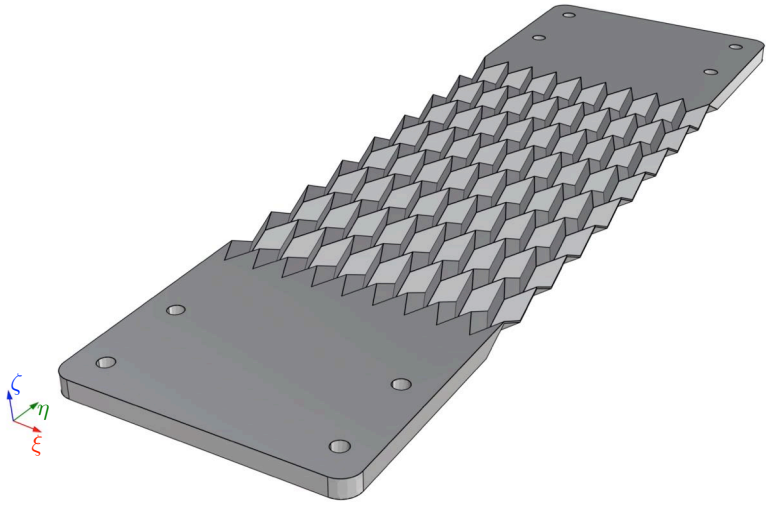


**Figure 4:** *Specimen geometry that has been used for testing the modal response.*

for the tensile tests: this technique gives remarkable advantages in displacement and strain field measurements. The modal response has been evaluated using Time Averaged Speckle Interferometry, a specifically developed interferometric approach for acquiring the vibration modes of objects.

### *3.1. Digital Image Correlation in Tensile Tests*

Digital Image Correlation is an optical technique that estimates the displacement field over an object's surface by correlating two images acquired before and after the motion. In its standard formulation (local approach), the images are partitioned into small sub-regions, called subsets. Thus, DIC applies to bi-dimensional (DIC-2D) and three-dimensional (DIC-3D) displacement fields on surfaces, as well as volumetric fields [40]. The fundamental hypothesis that holds the DIC approach is the optical flow constancy [40], defined as:

$$I(x, y, t) = I(x + u, y + v, t + \Delta t) \tag{9}$$

where $I(x, y, t)$ is the intensity field at point, defined by coordinates $(x, y)$, and at the time instant $t$. The terms $u$ and $v$ that are present in eq. (9) are, respectively, the $x$ and $y$ components of displacement, while $\Delta t$ is a discrete-time increment.

$$\frac{\partial I}{\partial t} + \frac{\partial I}{\partial x}\underbrace{\frac{\partial x}{\partial t}}_{\dot{u}} + \frac{\partial I}{\partial y}\underbrace{\frac{\partial y}{\partial t}}_{\dot{v}} = 0 \tag{10}$$

Eq. (10) is the first-order expansion of the relationship (9) second member, under the hypothesis of small displacements. The eq. (10) is a single equation with two unknowns ($\dot{u}$ and $\dot{v}$), which leads to an ill-posed problem. Several solutions have been proposed [41, 42], but the most used is the so called *Lucas-Kanade* approach [43]. This approach minimizes an error function, in which the displacements are modeled as an affine transformation.

$$u = a_0 + x_s + a_1 x_s + a_2 y_s + \overbrace{a_3 x_s^2 + a_4 x_s y_s + a_5 y_s^2}^{\text{parabolic terms}} \tag{11}$$

$$v = b_0 + y_s + b_1 x_s + b_2 y_s + \underbrace{b_3 y_s^2 + b_4 x_s y_s + b_5 x_s^2}_{\text{parabolic terms}} \tag{12}$$

Eqs. (11) and (12) are an example of parabolic shape functions that model an affine transform [40]. The coordinates $x_s$ and $y_s$ belong to a reference system attached to the subset center, while the parameter sets $\boldsymbol{a} = \{a_0, a_1, \dots a_n\}$ and $\boldsymbol{b} = \{b_0, b_1, \dots b_n\}$ represent the minimization aim.

$$\chi^2 = \sum_i \sum_j \left[R(i,j) - T(i+u, j+v)\right]^2 \tag{13}$$

The eq. (13) is the cost function, in which $R$ and $T$ are the reference and the target image, while $i$ and $j$ are indexes that define the pixel coordinates inside a subset whose center is in $(i_0, j_0)$. The cost function minimization requires posing to zero the derivatives, which are calculated with respect to the $\boldsymbol{a}$ and $\boldsymbol{b}$ parameter sets. This procedure leads to solve a system of the form $\boldsymbol{Ax} = \boldsymbol{c}$, in which $\boldsymbol{A} = \sum_k \boldsymbol{h}_k \boldsymbol{h}_k^T$ and $\boldsymbol{c} = \sum_k (R_k - T_k)\, \boldsymbol{h}_k$, where the vector $\boldsymbol{h}$ is defined as:

$$\boldsymbol{h} = \left\{ \frac{\partial T}{\partial x}, \frac{\partial T}{\partial y}, \frac{\partial T}{\partial x} x_s, \frac{\partial T}{\partial y} x_s, \dots \right\}$$

by assuming that parameters follows a sorting rule like $a_0, b_0, a_1, b_1, \dots, a_n, b_n$. The index $k$ moves on the whole image points involved in the calculation.

Therefore, expanding in series the second member of eq.(9) is not the only possible choice. Expanding the reference image [44, 45] $R$ gives remarkable advantages since it does not change during calculation history, as the intensity derivatives. In addition, this strategy is not sensitive to noise bias [46, 47]. An alternative solution is the expansion of both target and reference intensity fields at midpoint [48, 49].

The aforementioned local approach is the most common but is not the only one possible. The so-called global method uses the same course as the local one, but it differs by introducing a global function that describes the displacement field, instead of using the subset sampling [50, 51]. The global function is continuous, belonging to the $C_0$ class, although other choices have been proposed in literature [52, 53]. In this case, the region of interest (ROI) is discretized by a Finite Element-like mesh, where displacements depend on the nodal degrees of freedom, and are shared between neighboring elements [54]. Thus, the error function (13) can still be employed, but the parameter sets ($\boldsymbol{a}$ and $\boldsymbol{b}$) act now as nodal degrees of freedom [54].

Another remarkable advancement in the DIC world is the Integrated approach (iDIC) [55, 56]. The iDIC differs from the standard local method because of the shape functions: in this case, they are designed to match the problem-related displacement field, instead of using the general purpose ones. Problem-related shape functions make the domain partitioning useless: thus, the analysis procedure employs the whole pixels inside the ROI. Several examples of iDIC employment are residual stress [57] and fracture mechanics [58]: the outputs are problem-related, leading to great advantage because the data do not need additional post-processing.

In this campaign, we use 2D-DIC software with a local approach developed by one of the authors (A. Baldi). The specimens are tested under tensile load using an MTS Landmark 370 universal test machine (Figure 5b), with a load capacity of $\pm 100\,\text{kN}$ and a load cell with the same measurement range. The tests are conducted in displacement control. The images have been acquired using an Allied Vision Pike F421b (Figure 5c), with a resolution of $2048 \times 2048$ and a pixel size of $7.4\,\mu\text{m}$, and it is equipped with a Schneider macro lens. The synchronization

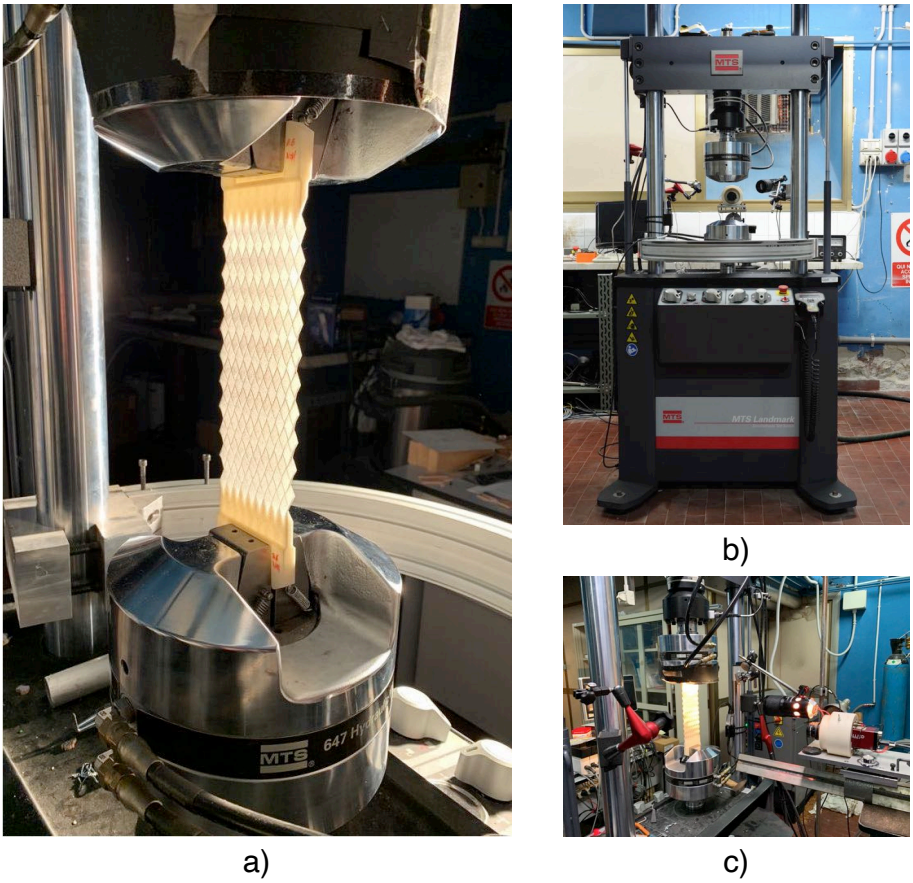


**Figure 5:** *Details of experimental setup. a) Sample of Miura-ori gripped in the test machine. b) MTS Landmark 370 universal testing machine. c) Overview of the camera setup with the lighting system.*

between the tensile test and the image acquisition is accomplished through a National Instrument board that sends a trigger signal to the camera at a fixed sampling rate.

### *3.2. Time-Averaged Speckle Interferometry for Modal Response*

Time-Averaged Speckle Interferometry is an interferometric technique developed for investigating the modal response of a vibrating object [59–63].

Figure 6a shows the interferometric setup employed for the mode measurement. The small angle between the object beam $I_O$ and the CCD axis ($\sim 10°$) leads to an almost out-of-plane displacement sensitivity. The laser source is a Helium-Neon tube with a wavelength of 632.7 nm and 50 mW power. The CCD is an Allied Vision Pike F421b, with the same characteristics reported in the DIC section, and it is equipped with a Schneider macro optics. The setup differs from conventional ones only by the reference branch: the reference beam is focused through a lens on the iris aperture plane of the CCD optics. Although this feature raises the alignment complexity (i.e., the CCD sensor must be fully enlightened), it has the remarkable advantages of using an high-quality lens [64] and simplifying the speckle field focusing. The phase-shifting is pursued using the PZT-actuated mirror on the reference branch. The specimen gripping system is a fixed-center vice (Figure 6b), with one harm modified for embedding the excitation system. The latter is composed by a solid-state elastic spring, actuated by PZT stack element.

The interference field is expressed by the following relationship:

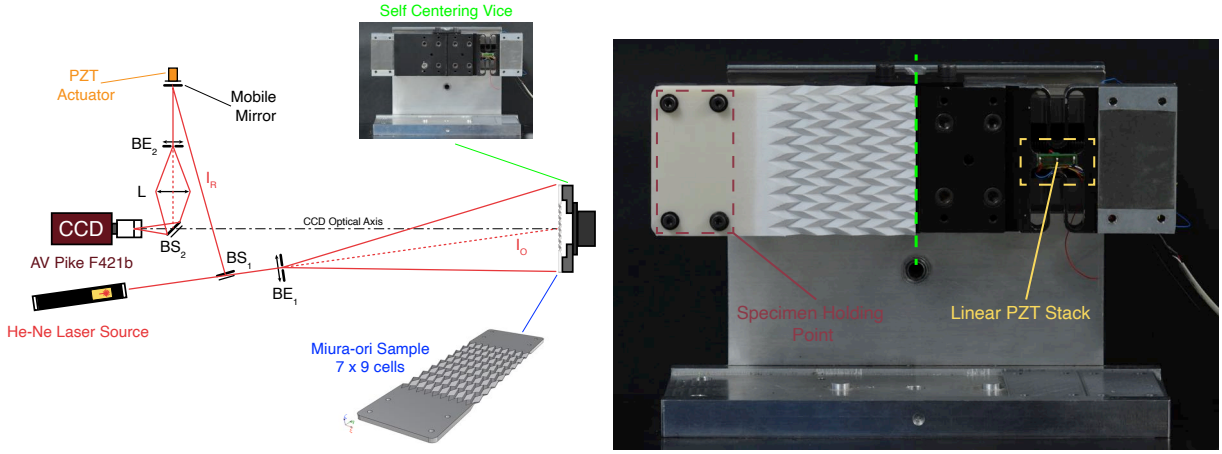


**(a)** *Interferometric setup.* **(b)** *Gripping/excitation system.*

**Figure 6:** *Time-Averaged Speckle setup. a) Scheme of the interferometric setup ($I_R$: Reference beam. $I_O$: Object Beam. BS: Beam Splitter. BE: Beam Expander. L: Lens). b) Fixed center vice, modified to embed the excitation system.*

$$I(x,y,t) = I_O + I_R + 2\sqrt{I_O I_R}\cos\left(\phi + \Delta\right) \tag{14}$$

Where $I_O$ and $I_R$ are respectively the object and the reference beam, $\phi = \phi(x,y)$ is the phase field. The term $\Delta = \Delta\left(x,y,t\right)$ needs special attention: it depends on either vibration amplitude $A$ and angular frequency $\omega$, illumination angle $\theta$, and the coherent source wavelength $\lambda$.

$$\Delta(x,y,t) = \frac{2\pi\left[1+\cos(\theta)\right]\left[A\cos(\omega t)\right]}{\lambda} \tag{15}$$

The intensity (14) is integrated by the CCD over the shutter aperture time $\tau$, leading to an output voltage $V_{\mathrm{CCD}}$ (16), where the term $\Gamma$ depends on the CCD gain and chromatic sensitivity [64].

$$V_{\mathrm{CCD}} = \Gamma\int_{t_0}^{t_0+\tau} I_O + I_R + 2\sqrt{I_O I_R}\cos\left(\phi+\Delta\right) \quad \text{where} \quad \tau = nT + \delta \tag{16}$$

In eq. (16), the term $\tau$ is defined as an integer number $n$ of vibration period $T = \frac{2\pi}{\omega}$ and a remainder $\delta$ that arises from the division $\frac{\tau}{T}$. The CCD output voltage (16) can be expanded in a convenient series form [63].

$$\begin{aligned} V_{\mathrm{CCD}} \propto \frac{2n\pi}{\omega}\left[I_O + I_R + 2\sqrt{I_O I_R}J_0(k)\cos(\phi)\right] + \\ + \delta\left\{I_O + I_R + 2\sqrt{I_O I_R}\left[\cos(\phi) - \frac{k\sin(\delta\omega)}{\delta\omega}\sin(\phi) - \frac{k^2\sin(2\delta\omega)}{\delta\omega}\cos(\phi) + \ldots\right]\right\} \\ \text{where} \quad k = \frac{2\pi A\left[1+\cos(\theta)\right]}{\lambda} \end{aligned} \tag{17}$$

The second member of eq. (17) is modulated by $\delta$: as the vibration frequency increases, the term $\delta$ decays[1], leading to the loss of relevance of the eq.(17) second member [63].

[1] The term $\delta$ is, therefore, the time delay between the shutter opening time, and the temporal interval the system needs to accomplish an integer number of oscillations.

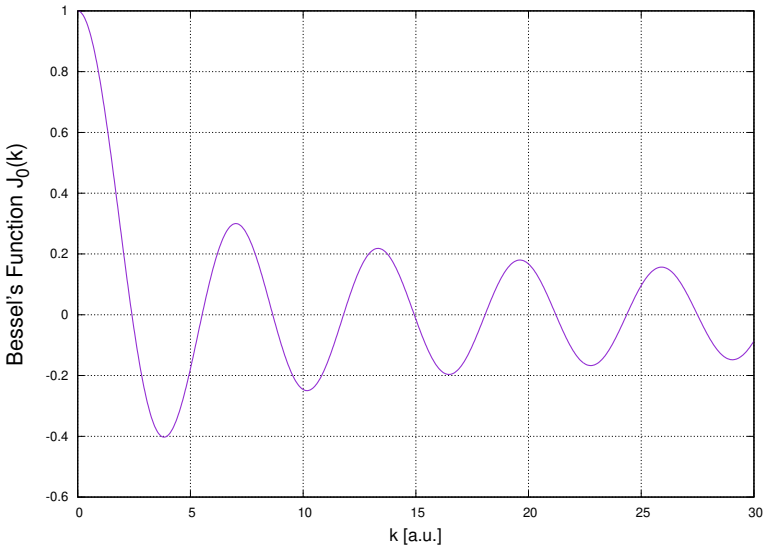


**Figure 7:** *$J_0$ Bessel's function.*

Thus, the first member of the (17) contains the $0^{\text{th}}$-order Bessel's function (Figure 7) and the term $k$, which essentially depends on the vibration amplitude $A$ because the illumination angle and the wavelength are intrinsic parameters of the setup. The fringes intensity field is modulated by $J_0$ Bessel's function (eq.(17)): thus, the nodes, where the amplitude $A$ is null, are characterized by the brightest fringe (if $A = 0$, then $J_0 = 1$). In addition, as the frequency $\omega$ increases, the amplitude $A$ decreases, with the consequent loss of contrast between fringes.

In Time-Averaged Speckle Interferometry, the acquisition method can follow two different strategies. The first consists of applying a phase-shifting approach [65] when the sample under analysis is at rest and then under the desired frequency excitation. The interferogram is obtained by subtracting the modulo $2\pi$ phase fields, leading to an almost binary fringe pattern [66]. A second possibility is to discard the phase modulo $2\pi$ [64] of the phase-shifting post-processing and focus only on the modulation (fringe intensity field). If the illumination is constant, the points with the same vibration amplitude have the same modulation. In this perspective, for each fringe that comes from the modulo $2\pi$ approach, there will be two Bessel's fringe: this is a consequence of the $J_0$ modulation (Figure 7), where at each peak corresponds two nodes. The advantages of this second method are the absence of a reference field and the immediate visibility of the fringe pattern [64], which comes from the modulation field only.

We employ the second approach because of its convenience. A Miura-ori specimen, reshaped as reported in Figure 4 for fitting in the gripping system, is excited through a frequency sweep with a constant amplitude. The specimen response has been monitored via a PZT transducer, bonded on the specimen surface. The PZT signal is acquired for identifying the resonant conditions, which are the main focus of the investigation. The interference field is then acquired and processed through the 5-frame Hariharan approach [65], focusing on the fringe visibility to obtain Bessel's fringe pattern.

## 4. Results

In this section, the results from the experimental tests are reported for the parametric analysis under tensile load and the modal response.

*4.1. Parametric Analysis on Thickness under Tensile Tests*

The experimental campaign for assessing the effect of thickness on the auxetic behavior of the Miura-ori geometry has been conducted on two sets of samples: one made of PLA and the other of ABS. The specimen geometry follows the specification of section 2, and the thickness is defined as the distance between the top and bottom surfaces of the faces. The images for the DIC analysis have been acquired in the linear elastic regime only, and the Poisson's ratio $\nu_{\eta\xi}$ is evaluated by the ratio of the $\varepsilon_\xi$ and $\varepsilon_\eta$, averaged on a mask of $7 \times 7$ cells, centered on the central one.

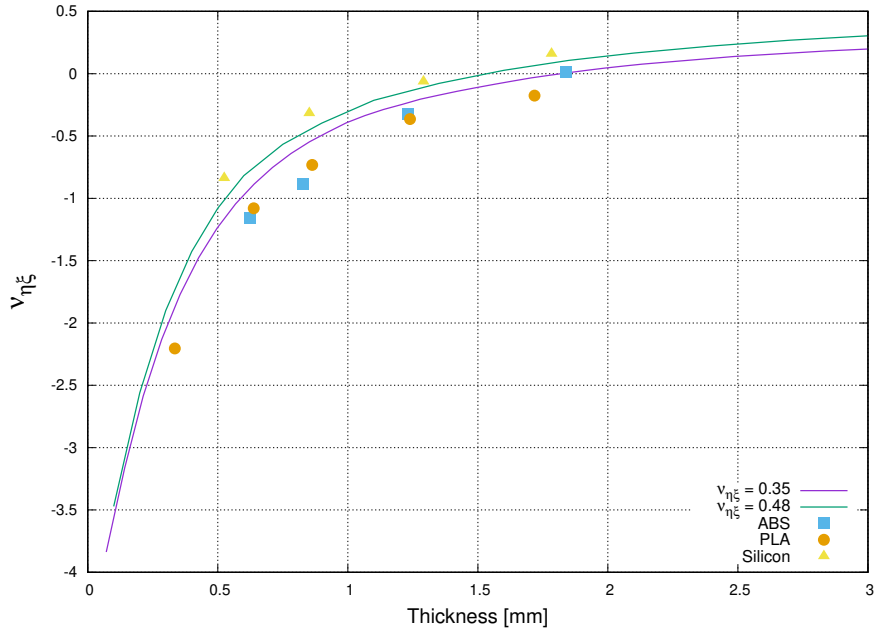


**Figure 8:** *Parametric analysis on thickness: comparison between experimental data an numerical simulation*

Figure 8 presents the data from the experimental observations, besides numerical simulation curves, used as a comparison. Both PLA and ABS have a Poisson's ratio of 0.35. Although the experimental data follow the numerical curve trend, a deviation occurs. During the fabrication, the specimens have been printed by filament deposition, which is oriented in the same direction for each layer. This consideration leads to the introduction of an anisotropic behavior of the samples. The validation has been pursued by developing a new Miura-ori specimen set made of silicon rubber: the latter has been poured into a mold to ensure an isotropic behavior of the samples. Therefore, the data relative to the silicon specimens, reported in Figure 8, are closer to the relative numerical curve, suggesting that the fabrication-induced anisotropy plays a not negligible role in mechanical response.

Figure 9 shows the displacement and strain fields of a PLA specimen with a thickness of 0.853 mm, that exhibits a Poisson's ratio of $-0.73$. The load has been applied in the negative direction of $\eta$ axis. Therefore, Figure 9a reports the $\xi$ component of displacement, which clearly shows the auxetic behavior. The data analysis and post-processing have been conducted using the software ABc developed by A. Baldi.

*4.2. Modal Response*

The modal response has been evaluated following the procedures explained in section 3.2. The shutter aperture time has been 50 ms. The specimen has been made of PLA and is 0.34 mm

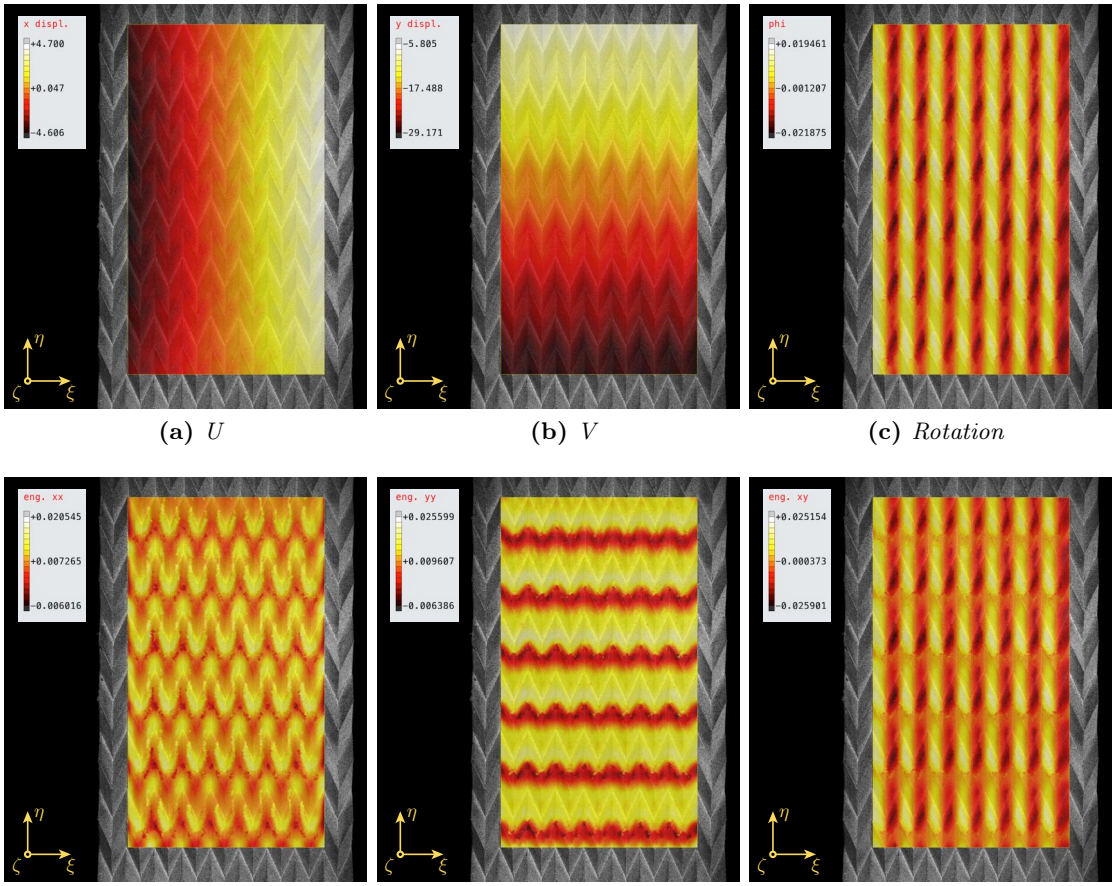


**(a)** $U$ **(b)** $V$ **(c)** *Rotation*

**(d)** $\varepsilon_{\xi\xi}$ **(e)** $\varepsilon_{\eta\eta}$ **(f)** $\varepsilon_{\xi\eta}$

**Figure 9:** *Results of DIC analysis on a PLA specimen 0.853 mm thick.*

thick. A thin layer of varnish has been applied on the sample surface to avoid any transparency effect.

Figure 10 reports the experimental results that come from the Time-Averaged Speckle Interferometry. The numerical resonant modes, calculated with the Finite Element, are used as a comparison. The interferograms give qualitative information about the shape of resonant modes, which agree with the numerical predictions. The small deviation observed between the experimental and numerical resonant frequencies can be addressed to the varnish layer or to the boundary conditions.

## 5. Discussion

The parametric analysis of the thickness influence on the auxetic response of Miura-ori geometry shows that the global Poisson's ratio $\nu_{\eta\xi}$ strongly depends on the thickness. The experimental data from DIC analysis fits the numerical simulations trend, even though the deviation is due to fabrication anisotropy. The silicon rubber specimen plays a fundamental role in identifying the source of the bias between numerical and experimental data. DIC proved to be a consolidated technique for measuring displacement and strain field, even for challenging geometry such as the Miura-ori one.

Time-averaged speckle interferometry is a remarkable technique for analyzing the modal

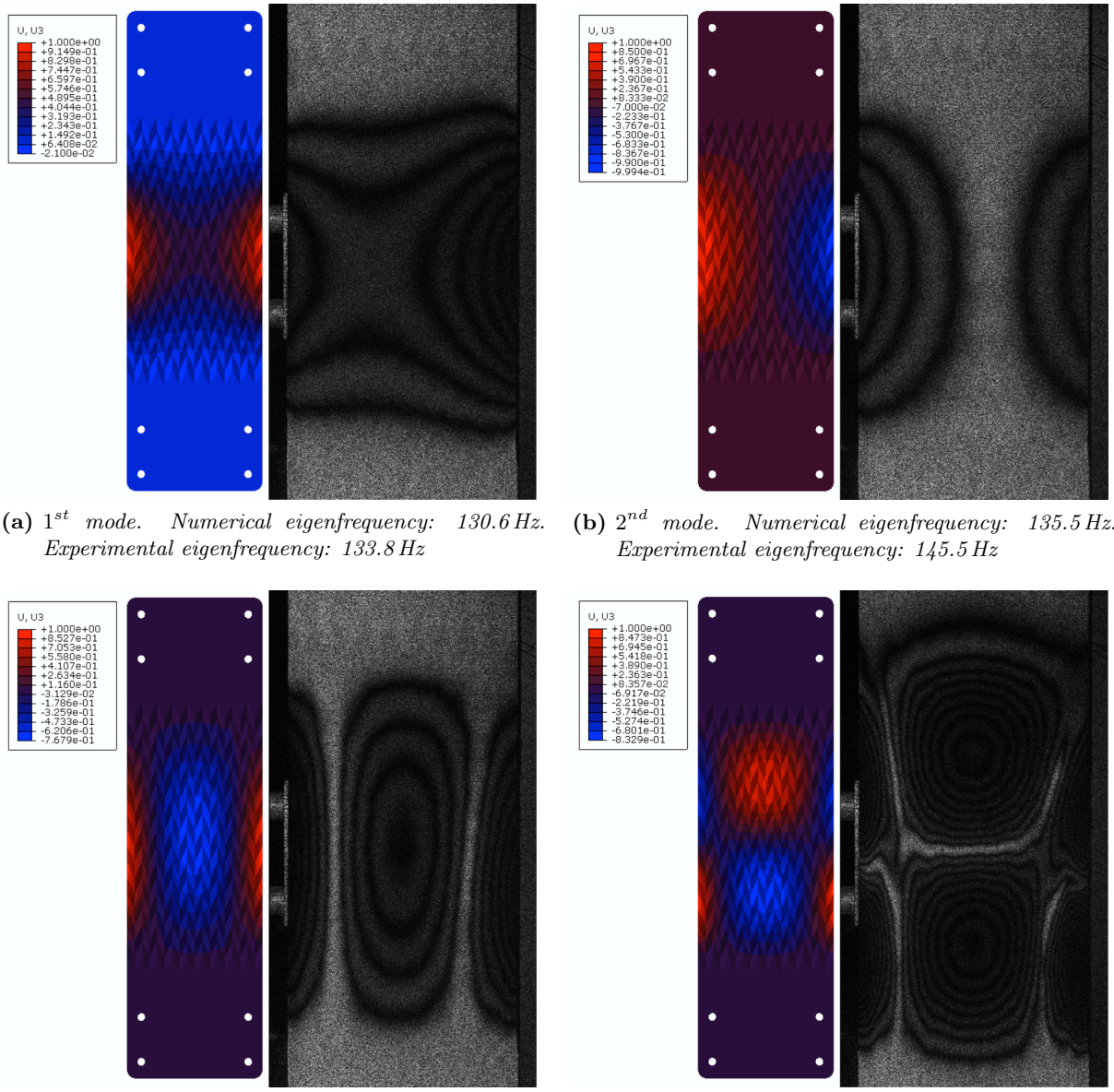


**(a)** $1^{st}$ *mode. Numerical eigenfrequency: 130.6 Hz. Experimental eigenfrequency: 133.8 Hz*

**(b)** $2^{nd}$ *mode. Numerical eigenfrequency: 135.5 Hz. Experimental eigenfrequency: 145.5 Hz*

**(c)** $3^{rd}$ *mode. Numerical eigenfrequency: 294.5 Hz. Experimental eigenfrequency: 321.0 Hz*

**(d)** $4^{th}$ *mode. Numerical eigenfrequency: 558.7 Hz. Experimental eigenfrequency: 602.0 Hz*

**Figure 10:** *Comparison between the resonant modes of a Miura-ori structure acquired with the Time-Averaged Speckle Interferometry and numerical simulations.*

response of a vibrating object. Thus, it avoids the more expensive high-speed cameras or laser vibrometers. The experimental interferograms exhibit a closer shape with respect to the numerical predictions: this poses the basis for further investigation on the Miura-ori modal properties.

## References

[1] Evans K E 1991 *Endeavour* **15** 170–174
[2] Lakes R S and Elms K 1993 *Journal of Composite Materials* **27** 1193–1202
[3] Evans K and Alderson K 2000 *Engineering Science & Education Journal* **9** 148–154

[4] Alderson A and Alderson K L 2007 *Proceedings of the Institution of Mechanical Engineers, Part G: Journal of Aerospace Engineering* **221** 565–575
[5] Veronda D R and Westmann R A 1970 *Journal of Biomechanics* **3** 111–124
[6] Lees C, Vincent J F V and Hillerton J E 1991 *Bio-Medical Materials and Engineering* **1** 19–23
[7] Timmins L H, Wu Q, Yeh A T, Moore J E and Greenwald S E 2010 *American Journal of Physiology-Heart and Circulatory Physiology* **298** H1537–H1545
[8] Baughman R H, Shacklette J M, Zakhidov A A and Stafström S 1998 *Nature* **392** 362–365
[9] Goldstein R V, Gorodtsov V A and Lisovenko D S 2010 *Mechanics of Solids* **45** 529–545
[10] Lubarda V A and Meyers M A 1999 *Scripta Materialia* **40** 975–977
[11] Cabras L and Brun M 2014 *Proceedings of the Royal Society A: Mathematical, Physical and Engineering Sciences* **470** 20140538
[12] Cabras L and Brun M 2016 *Journal of the Mechanics and Physics of Solids* **91** 56–72
[13] Lakes R 1987 *Science* **235** 1038–1040
[14] Choi J B and Lakes R S 1992 *Journal of Materials Science* **27** 4678–4684
[15] Peng X L, Soyarslan C and Bargmann S 2020 *Extreme Mechanics Letters* **35** 100641
[16] Zhang X Y, Ren X, Zhang Y and Xie Y M 2022 *Thin-Walled Structures* **174** 109162
[17] Grima J N and Gatt R 2010 *Advanced Engineering Materials* **12** 460–464
[18] Carta G, Brun M and Baldi A 2016 *Mechanics of Materials* **97** 67–75
[19] Carta G, Cabras L and Brun M 2016 *Journal of the European Ceramic Society* **36** 2183–2192
[20] Baldi A, Brun M and Carta G 2022 *Mechanics of Materials* **164** 104114
[21] Theocaris P S, Stavroulakis G E and Panagiotopoulos P D 1997 *Archive of Applied Mechanics* **67** 274–286
[22] Mizzi L, Mahdi E M, Titov K, Gatt R, Attard D, Evans K E, Grima J N and Tan J C 2018 *Materials & Design* **146** 28–37
[23] Bertoldi K, Reis P M, Willshaw S and Mullin T 2010 *Advanced Materials* **22** 361–366
[24] Shen J, Zhou S, Huang X and Xie Y M 2014 *physica status solidi (b)* **251** 1515–1522
[25] Khan K A, Alshaer M H and Khan M A 2021 *Advanced Engineering Materials* **23** 2001041
[26] Saxena K K, Das R and Calius E P 2016 *Advanced Engineering Materials* **18** 1847–1870
[27] Ren X, Das R, Tran P, Ngo T D and Xie Y M 2018 *Smart Materials and Structures* **27** 023001
[28] Prawoto Y 2012 *Computational Materials Science* **58** 140–153
[29] Miura K and Pellegrino S 2020 *Forms and Concepts for Lightweight Structures* (Cambridge University Press)
[30] Miura K 1985 *The Institute of Space and Astronautical Science report* **618** 1–9
[31] Zhang C, Yang Q and Tao R 2021 *Smart Materials and Structures* **30** 075004
[32] Lv C, Krishnaraju D, Konjevod G, Yu H and Jiang H 2014 *Scientific Reports* **4** 5979
[33] Tolman S S, Delimont I L, Howell L L and Fullwood D T 2014 *Smart Materials and Structures* **23** 094010
[34] Liu S, Lu G, Chen Y and Leong Y W 2015 *International Journal of Mechanical Sciences* **99** 130–142
[35] Pydah A and Batra R C 2017 *Thin-Walled Structures* **115** 311–322
[36] Xiang X M, You Z and Lu G 2018 *Composite Structures* **195** 359–374

[37] Schenk M and Guest S D 2013 *Proceedings of the National Academy of Sciences* **110** 3276–3281

[38] Wei Z Y, Guo Z V, Dudte L, Liang H Y and Mahadevan L 2013 *Physical Review Letters* **110** 215501–

[39] Moradweysi P, Santucci P M, Carta G, Goudarzi T, Aghdam M M, Baldi A and Brun M 2022 *Mechanics of Advanced Materials and Structures* 1–19

[40] Schreier H, Orteu J J, Sutton M A *et al.* 2009 *Image Correlation for Shape, Motion and Deformation Measurements* vol 1 (Springer New York, NY)

[41] Horn B K P and Schunck B G 1981 *Artificial Intelligence* **17** 185–203

[42] Bruhn A, Weickert J and Schnörr C 2005 *International Journal of Computer Vision* **61** 211–231

[43] Lucas B D and Kanade T 1981 An iterative image registration technique with an application to stereo vision *IJCAI'81: 7th international joint conference on Artificial intelligence* vol 2 (Vancouver, Canada) pp 674–679

[44] Shum H Y and Szeliski R 1998 Construction and refinement of panoramic mosaics with global and local alignment *Proceedings of the IEEE International Conference on Computer Vision* pp 953–958

[45] Baker S and Matthews I 2004 *International Journal of Computer Vision* **56** 221–255

[46] Shao X, Dai X and He X 2015 *Optics and Lasers in Engineering* **71** 9–19

[47] Baldi A, Santucci P M and Bertolino F 2022 *Optics and Lasers in Engineering* **154** 107012

[48] Davis C Q and Freeman D M 1998 *Optical Engineering* **37** 1290–1298

[49] Tong W 2013 *Strain* **49** 313–334

[50] Sun Y, Pang J H L, Wong C K and Su F 2005 *Applied Optics* **44** 7357–7363

[51] Hild F and Roux S 2006 *Strain* **42** 69–80

[52] Cheng P, Sutton M A, Schreier H W and McNeill S R 2002 *Experimental Mechanics* **42** 344–352

[53] Roux S, Hild F and Berthaud Y 2002 *Applied Optics* **41** 108–115

[54] Baldi A and Bertolino F 2016 *Meccanica* **51** 979–991

[55] Roux S and Hild F 2006 *International Journal of Fracture* **140** 141–157

[56] Gao J and Shang H 2009 *Applied Optics* **48** 1371–1381

[57] Baldi A 2014 *Experimental Mechanics* **54** 379–391

[58] Baldi A and Santucci P M 2022 *Engineering Fracture Mechanics* **259** 108082

[59] Tiziani H J and Klenk J 1981 *Applied Optics* **20** 1467–1470

[60] Joenathan C 1991 *Applied Optics* **30** 4658–4665

[61] Li X and Tao G 2002 *Optics & Laser Technology* **34** 259–264

[62] Romero G, Alvarez L, Alanís E, Nallim L and Grossi R 2003 *Optics and Lasers in Engineering* **40** 81–90

[63] Wang W C, Hwang C H and Lin S Y 1996 *Applied Optics* **35** 4502–4509

[64] Baldi A, Jacquot P and Ginesu F 2004 Una applicazione della tecnica speckle all'analisi di uno statore per piezo-motors *Atti del XXXIII Convegno AIAS*

[65] Creath K, Crennel K M, Gåsvik K J, Halliwell N A, Pickering C J, Hariharan P, Kujawinska M and Yatagai T 1993 *Interferogram analysis: digital fringe pattern measurement technique* (IOP Publishing)

[66] Borza D N 2004 *Optics and Lasers in Engineering* **41** 515–527